

Modelling the deformation mechanisms, structure–property relationships and applications of auxetic nanomaterials

A. Alderson^{*,1}, K. L. Alderson¹, K. E. Evans², J. N. Grima³, M. R. Williams¹, and P. J. Davies¹

¹ Centre for Materials Research and Innovation, Bolton Institute, Bolton BL3 5AB, UK

² Department of Engineering, University of Exeter, Exeter EX4 4QF, UK

³ Department of Chemistry, University of Malta, Msida MSD 06, Malta

Received 7 July 2004, accepted 29 November 2004

Published online 15 February 2005

PACS 62.25.+g, 64.70.Kb, 81.07.Bc

Analytical and Molecular Mechanics methods have been used to study the structure and deformation mechanisms acting at the molecular level in the auxetic polymorph of crystalline silica (α -cristobalite). The Molecular Mechanics simulations indicate a stress-induced phase transition from α -cristobalite to ‘ordered’ β -cristobalite occurs for uniaxial loading along the x_3 direction. This is in reasonable agreement with the previous prediction from an analytical model assuming deformation is by concurrent dilation and cooperative rotation (about axes in the x_1 - x_2 plane, passing through the midpoints of opposing edges – the a -axes) of the SiO_4 tetrahedral molecular sub-units, previously shown to predict the Poisson’s ratio for loading in the x_3 direction. The analytical models have been extended to include cooperative rotation of each tetrahedron about its axis (the c -axis) mostly closely aligned with the principal unit-cell x_3 -axis. The new models enable significantly improved prediction of the Poisson’s ratios of α -cristobalite when loaded in one of the transverse (x_1 or x_2) directions. Parametric fitting of the analytical models indicate that the deformation mechanism for transverse uniaxial loading of α -cristobalite is by concurrent dilation and cooperative rotation about the local a and c -axes of the SiO_4 tetrahedra.

© 2005 WILEY-VCH Verlag GmbH & Co. KGaA, Weinheim

1 Introduction

Negative Poisson’s ratio (ν) materials and structures expand transversely when stretched axially, and also undergo transverse contraction under axial compression. This is shown in Fig. 1, along with the classic example of a re-entrant honeycomb structure deforming by hinging of the cell walls leading to negative Poisson’s ratio behaviour. There is increasing interest in the development of these novel materials, known as *auxetic* materials [1], due to their counter-intuitive behaviour and also in applications where the auxetic property itself, or enhancements in other materials properties due to a negative Poisson’s ratio, may be exploited. For example, auxetic honeycomb and foam materials have been shown to offer enhanced de-fouling or tunable size selectivity when employed as filter materials, due to the characteristic high volume change (and hence permeability variation) which they undergo upon mechanical loading [2].

The development of auxetic nanomaterials is expected to lead to high modulus auxetic materials as well as leading to potential applications in sensor, molecular sieve and separation technologies. For example, we have recently reported that a number of zeolitic cage structures are predicted by molecular modelling calculations to be auxetic [3]. Zeolites are polyhedral aluminosilicate framework nanostruc-

* Corresponding author: e-mail: A.Alderson@bolton.ac.uk

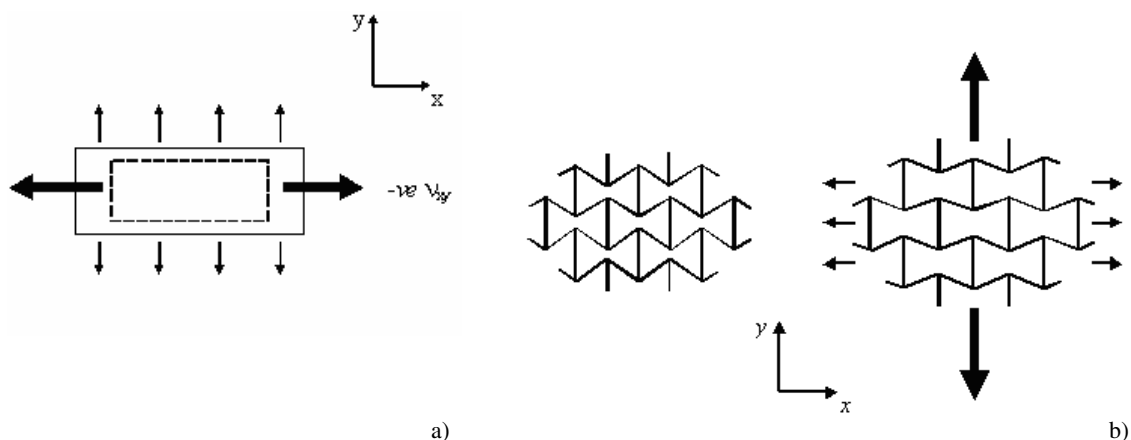


Fig. 1 (a) Schematic of a material displaying negative Poisson's ratio (auxetic) behaviour; (b) a re-entrant honeycomb undergoing deformation by hinging of the cell walls, leading to negative Poisson's ratio behaviour.

tures commonly used as molecular sieves because of their availability and well-defined molecular-sized cavities and pathways. Zeolite MFI was predicted by the force-field simulations to have both positive and negative ν 's for loading in the z -direction ($\nu_{zx} = -0.35$ and $\nu_{zy} = +0.38$). Combined molecular modelling and Monte Carlo simulations for the strain-dependent sorption of benzene and neopentane molecules onto the MFI all-silica zeolite nanostructure undergoing uniaxial loading along the z -direction were performed, and demonstrated that the benefits in separation applications due to auxetic functionality were predicted to persist down to the nanoscale [3].

One of the first attempts to design materials displaying negative Poisson's ratio behaviour at the molecular level was based on an idealised 2D system of hard cyclic hexamers [4]. This was followed by the modelling of auxetic behaviour in molecular networks designed by scaling down geometries known to lead to auxetic behaviour at the macroscale. An example of this approach is the design of nanoscale macrocyclic hydrocarbons based on the re-entrant honeycomb geometry known to lead to auxetic behaviour at the macroscale [2, 5] (Fig. 2). Molecular modelling has been used to predict auxetic behaviour in these theoretical nanomaterials [1]. Analytical models have also been developed, extending the cell wall flexure model of honeycomb deformation [5], to include cell wall hinging and stretching acting concur-

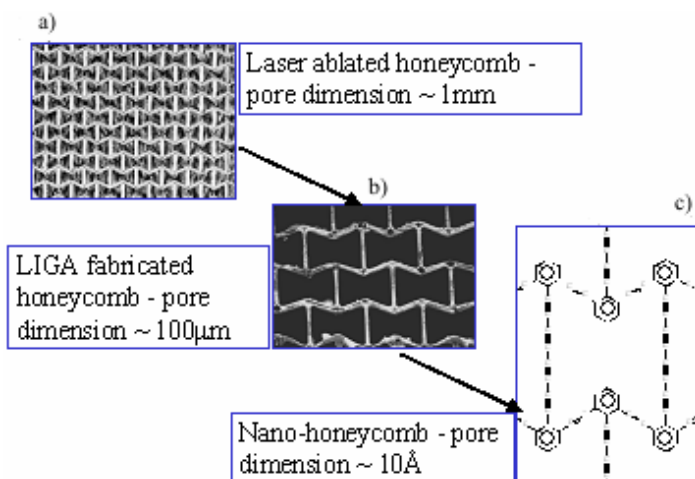


Fig. 2 (online colour at: www.pss-b.com) Re-entrant honeycomb networks: (a) macroscale polymeric honeycomb [2]; (b) microscale metallic honeycomb structure; (c) theoretical polyacetylene molecular honeycomb network sub-unit [1].

rently with cell wall flexure, and also taking account of the inhomogeneity (atomic bond structure) that exists in the honeycomb cell walls at the nanoscale [6]. These more advanced analytical models for honeycomb deformation were shown to lead to excellent agreement with the molecular model calculations which, when used in combination with the molecular modelling approach, enable an efficient route to the design of this family of network nanostructures with tailored mechanical properties.

Little progress has been reported on the synthesis of the molecular re-entrant sub-units required for auxetic behaviour. However, whilst the synthesis of auxetic nanomaterials remains a challenge, it is likely that advances in supramolecular chemistry and crystal engineering will soon overcome this. Perhaps the most promising route to date in the development of man-made auxetic nanomaterials is proposed to be due to site-connectivity-driven rod orientation in a main-chain liquid crystalline polymer [7].

An alternative approach is to model the behaviour of naturally-occurring molecular-level auxetic materials in order to improve the design of chemically synthesisable auxetic nanomaterials. We have reported [8] the development of analytical expressions for the Poisson's ratios of certain silica polymorphs which reproduce the experimental values for loading in the x_3 direction remarkably well, explaining in the process the dichotomy between negative and positive values of Poisson's ratio in α -cristobalite [9] and α -quartz [10], respectively. The models consist of deformation due to cooperative rotation (described elsewhere as a 'rigid unit mode' (RUM) [11, 12]) and dilation of the SiO_4 tetrahedra making up the framework nanostructure of these materials. Most recently, the analytical models have been extended to predict a uniaxial stress-induced second phase, and Molecular Mechanics simulations have been performed to investigate the effects of uniaxial stress and pressure on the structure and mechanical properties for α -cristobalite [13].

This paper reports further results from our recent modelling investigations into the structure, deformation mechanisms and mechanical properties of α -cristobalite in order to develop an increased understanding of auxetic deformation mechanisms acting in a nanomaterial.

2 Models

2.1 Molecular mechanics model

The *Cerius*² Molecular Modelling software (Accelrys) was employed on a Silicon Graphics O2 workstation. The starting structure for α -cristobalite was as provided within the *Cerius*² structure database derived from experimental data. The modelling protocols for the structure and mechanical properties simulations were as described in detail in Ref. [3]. For the work reported here, the Burchart force-field [14], developed specifically for silicas and aluminophosphates, was employed in the structure and mechanical properties simulations. The Burchart force-field assumes the frameworks are largely covalent and interactions were parameterised using experimental data. Whilst this force-field does not reproduce the negative on-axis Poisson's ratios known to occur in α -cristobalite, it does predict low positive values and also gives reasonable agreement with the experimental on-axis Young's moduli. The stiffness matrix \mathbf{C} was computed from the second derivative of the energy expression, and the on-axis Poisson's ratios and other elastic constants were obtained directly from the compliance matrix, $\mathbf{S} = \mathbf{C}^{-1}$, since, for example, $\nu_{ij} = s_{ij}/s_{ii}$.

Structure and mechanical properties simulations were performed for uniaxial loading along each of the mutually orthogonal principal axes x_1 , x_2 and x_3 .

2.2 Analytical models

The basic molecular 'building block' for α -cristobalite is the SiO_4 tetrahedron consisting of an O atom at each of the four corners surrounding a central Si atom. The molecular structure consists of a framework of corner-sharing SiO_4 tetrahedra in which each O atom is shared between two adjacent tetrahedra. Figure 3(a) shows the cartesian coordinate system and unit cell (space group P4₁2₁2) for α -cristobalite, which is characterized by a 'tilt' (by an angle $\delta = 23.5^\circ$) of the tetrahedra about the local axis passing

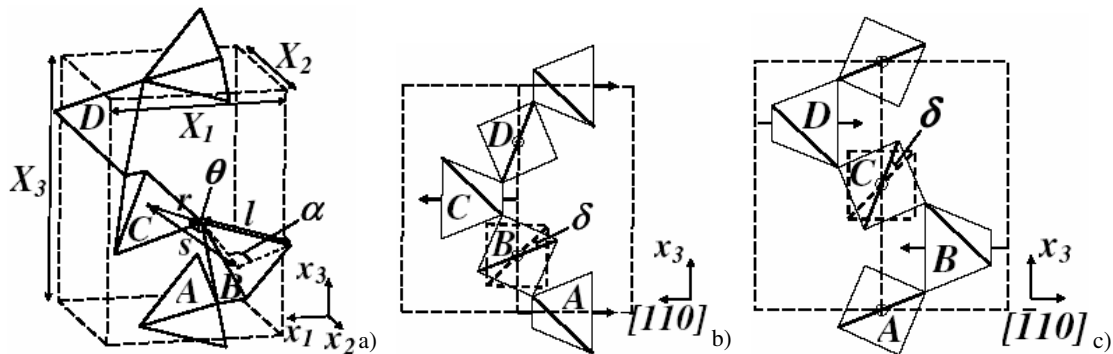


Fig. 3 a) Unit cell and cartesian coordinates for α -cristobalite. b) $x_3 - [\bar{1}10]$ projection of the unit cell, showing tetrahedral axes and ‘untilted’ tetrahedron (B) to define tilt angle δ . c) $x_3 - [\bar{1}10]$ projection of the unit cell.

through the midpoints of opposing tetrahedron edges and lying within the x_1 - x_2 plane for each tetrahedron (Figs. 3(b) and 3(c)).

Figure 4(a) shows the projection of the unit-cell in the x_1 - x_2 plane, again with the tilt axes in the x_1 - x_2 plane indicated. The projection of the ‘untilted’ ($\delta = 0$) structure in the x_1 - x_2 plane is shown in Fig. 4(b) and corresponds to the ‘idealised’ β -cristobalite structure (space group Fd3m) originally proposed by Wyckoff [15] for the high temperature phase of cristobalite. However, the idealised β -cristobalite structure contains collinear Si–O–Si bonds which are unusual in silica polymorphs. The actual structure of β -cristobalite remains a topic of some debate in the literature. One view is that β -cristobalite has a dynamically disordered framework in which the oxygen atoms precess about the Si–Si axes in the idealised structure [16]. Another suggestion is that the β -cristobalite structure is a dynamic average of domains of α -cristobalite [17]. Yet another suggestion for the structure of β -cristobalite proposes a locally ordered structure (‘ordered’ β -cristobalite) [18–20]. The ‘ordered’ β -cristobalite structure (space group $I\bar{4}2d$) is derived from the idealized β -cristobalite structure by rotation of each tetrahedron by an angle ϕ ($= 19.8^\circ$) about a tetrahedral axis aligned along the x_3 direction (i.e. perpendicular to the x_1 - x_2 plane) – Fig. 4(c).

A local tetrahedral co-ordinate system is defined in Fig. 5(a), comprising of 3 orthogonal axes, each passing through the midpoints of two opposing edges. The a -axis in the local coordinate system lies in the x_1 - x_2 plane of the cartesian coordinate system for α -cristobalite (Figs. 3(b), 3(c) and 4(a)). The local c -axis is aligned along the x_3 cartesian axis for the idealised/ordered β -cristobalite structures. In α -cristobalite, the local c -axis is rotated away from the x_3 axis due to the rotation of each tetrahedron by an angle δ about the a -axis (Fig. 5(b)).

Previously [21], analytical models have been developed which assume that the tetrahedral framework for α -cristobalite deforms by tetrahedral dilation (i.e. the O–O bond distance, l , varies – the Dilating Tetrahedra Model (DTM)), cooperative tetrahedral rotation about the local a -axes (δ varies – the Rotating

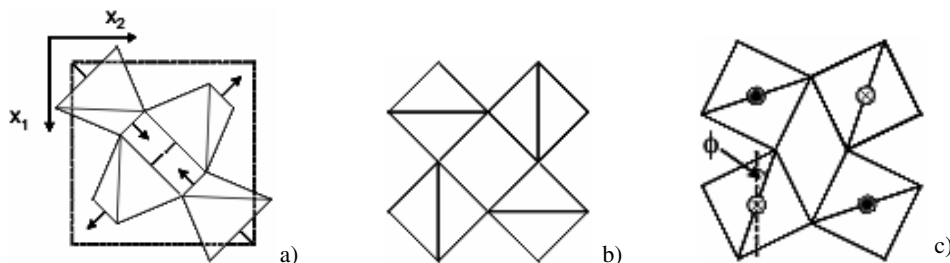


Fig. 4 x_1 - x_2 projections of: a) α -cristobalite, b) idealised β -cristobalite and c) ordered β -cristobalite.

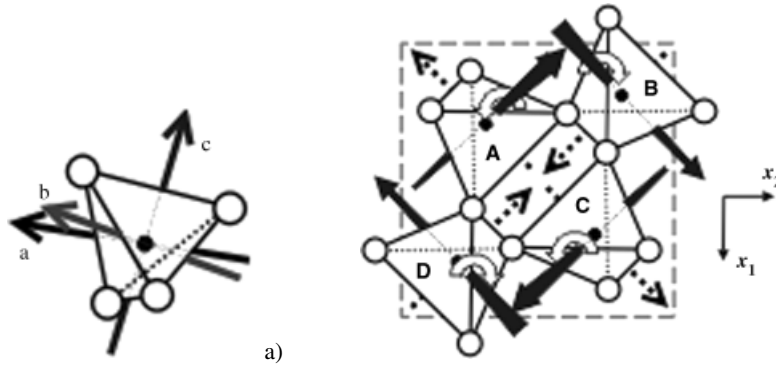


Fig. 5 a) Local orthogonal tetrahedral coordinate system; b) x_1 - x_2 projection of α -cristobalite, showing local tetrahedral a -axes (dashed arrows) and c -axes (solid arrows). Filled circles are Si atoms, empty ones are O atoms.

Tetrahedra Model 1 (RTM1)) and concurrent tetrahedral dilation and a -axis rotation (l and δ vary simultaneously – the Concurrent Tetrahedra Model 1 (CTM1)). Molecular mechanics simulations have confirmed that the mechanisms acting in the CTM1 occur for uniaxial loading of α -cristobalite in the x_3 direction [13]. However, molecular mechanics simulations for uniaxial loading of α -cristobalite in one of the transverse (x_1 or x_2) directions suggest an alternative tetrahedral rotation mechanism acts [13], resulting in 2 distinct values of the Si–O–Si intertetrahedral angle (θ) at any given stress level. We consider this is due to cooperative rotation of the tetrahedra about the local c -axes, shown in Fig. 5(b).

We have, therefore, recently developed 3 new analytical models incorporating cooperative rotation of the tetrahedra about the local c -axes [22]: cooperative tetrahedral rotation about the local c -axes (ϕ varies – the Rotating Tetrahedra Model 2 (RTM2)); concurrent tetrahedral dilation and c -axis rotation (l and ϕ vary simultaneously – the Concurrent Tetrahedra Model 2 (CTM2)); concurrent tetrahedral dilation, c -axis rotation and a -axis rotation (l , ϕ and δ vary simultaneously – the Concurrent Tetrahedra Model 3 (CTM3)). Full details are given in Ref. [22], but the method is summarized here.

The lengths of the unit cell, X_1 , X_2 and X_3 along the x_1 , x_2 and x_3 directions, respectively, are related to the tetrahedral size (l) and orientation angles (δ and ϕ) by [22]

$$X_1 = \sqrt{2}l [\sin (45 + \phi) + \cos (45 + \phi) \cos \delta], \quad (1)$$

$$X_2 = \sqrt{2}l [\cos (45 + \phi) + \sin (45 + \phi) \cos \delta], \quad (2)$$

$$X_3 = 2\sqrt{2}l \cos \delta. \quad (3)$$

Poisson's ratio is defined by:

$$\nu_{ij} = -\frac{d\varepsilon_j}{d\varepsilon_i} = -\frac{dX_j}{X_j} \frac{X_i}{dX_i}, \quad (4)$$

where ε_i is the strain in the x_i direction and $i, j = 1, 2$ or 3 ($i \neq j$). The infinitesimal changes in the lengths of the unit cell are given by:

$$dX_i = \frac{\partial X_i}{\partial l} dl + \frac{\partial X_i}{\partial \phi} d\phi + \frac{\partial X_i}{\partial \delta} d\delta. \quad (5)$$

In Eq. (5), $dl = d\delta = 0$ for the RTM2, and $d\phi = 0$ for the CTM2.

Table 1 Analytical model Poisson’s ratio expressions for α -cristobalite. $\kappa = l(d\delta/dl)$ and $\lambda = l(d\phi/dl)$.

model	$\nu_{12} = \nu_{21}$	$\nu_{13} = \nu_{23}$
DTM (l varying) [21]	-1	-1
RTM1 (δ varying) [21]	-1	$-\left(\frac{1 + \cos \delta}{\cos \delta}\right)$
CTM1 (l and δ varying) [21]	-1	$-\left(\frac{1 + \cos \delta}{\cos \delta}\right)\left(\frac{\cos \delta - \kappa \sin \delta}{1 + \cos \delta - \kappa \sin \delta}\right)$
RTM2 (ϕ varying)	+1	0
CTM2 (l and ϕ varying)	$\frac{[1 + \cos \delta + \lambda(\cos \delta - 1)]}{[1 + \cos \delta + \lambda(1 - \cos \delta)]}$	$-\frac{1}{1 + \lambda\left(\frac{1 - \cos \delta}{1 + \cos \delta}\right)}$
CTM3 (l, ϕ and δ varying)	$-\frac{[1 + \cos \delta + \lambda(\cos \delta - 1) - \kappa \sin \delta]}{[1 + \cos \delta + \lambda(1 - \cos \delta) - \kappa \sin \delta]}$	$-\left(\frac{1 + \cos \delta}{\cos \delta}\right)\left(\frac{\cos \delta - \kappa \sin \delta}{1 + \cos \delta + \lambda(1 - \cos \delta) - \kappa \sin \delta}\right)$

Table 1 contains the Poisson’s ratio expressions for uniaxial loading in the transverse directions (x_1 and x_2) of α -cristobalite for the 3 models described above, and also for the DTM, RTM1 and CTM1 models developed previously [21].

3 Results

3.1 σ_3 -induced phase change for cristobalite

Figure 6a shows the calculated unit-cell parameter variations with loading along x_3 , predicted from the molecular model simulations. The unit-cell dimension along the loading direction (X_3) decreases smoothly for compressive loading. The unit-cell length X_1 remains nearly constant for compressive loading, consistent with the low positive (near zero) value of ν_{31} calculated previously using the Burchart force-field [3]. In the case of tensile loading, X_3 increases smoothly along the same gradient as for compressive loading, and X_1 remains approximately unchanged, for $\sigma_3 < 1$ GPa. At a stress value within the range of $1 \text{ GPa} < \sigma_3 < 1.2 \text{ GPa}$ the unit-cell dimension variations with stress depart from the rate of change

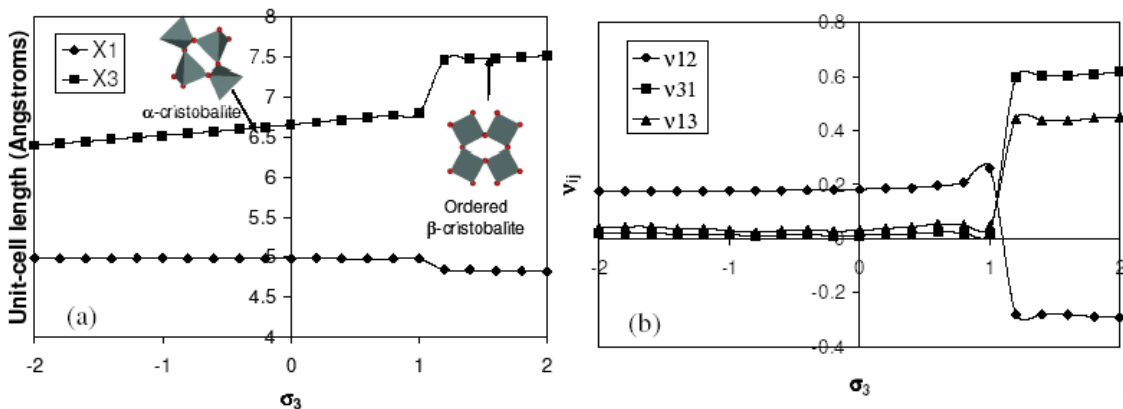


Fig. 6 (online colour at: www.pss-b.com) Molecular mechanics simulation data: (a) unit-cell lengths X_1 and X_3 versus σ_3 – inserts show x_1 - x_2 plane projections of unit-cell corresponding to α -cristobalite and ‘ordered’ β -cristobalite; (b) ν_{ij} versus σ_3 .

Table 2 Experimental, calculated analytical model and force-field simulation Poisson's ratios for transverse loading of α -cristobalite. Force-field simulation data are shown for the Burchart [14], BKS [26], Universal [27, 28] and CVFF [29] force-fields.

model	ν_{12}	ν_{13}
experiment [9]	+0.06	-0.10
DTM	-1	-1
RTM1	-1	-2.09
CTM1 ($\kappa = 5.18$) [8]	-1	-16.17
RTM2	+1	0
CTM2 ($\lambda = 35$)	+0.20	-0.40
CTM3 ($\lambda = 15.1, \kappa = 2.02$)	+0.06	-0.10
Burchart [3]	+0.20	+0.02
BKS [3]	+0.16	+0.07
Universal [3]	+0.11	+0.14
CVFF [3]	+0.09	-0.16

observed for $\sigma_3 < 1$ GPa, indicating a phase transition has occurred. The inserts in Fig. 6a show the x_1 - x_2 projections for the unit-cell and correspond to the α -cristobalite and 'ordered' β -cristobalite structures for the low tensile and high tensile stress regions, respectively. Figure 6b shows the predicted σ_3 -dependent Poisson's ratio behaviour from the molecular modeling simulations. The Poisson's ratios show a clear change in magnitude from one phase to the other, and include a change in sign of ν_{12} from positive (α -cristobalite) to negative ('ordered' β -cristobalite).

3.2 Deformation mechanisms for transverse loading of α -cristobalite

Table 2 summarises the Poisson's ratios calculated for transverse loading of α -cristobalite for the analytical models developed to date. Experimental values and values from previous force-field simulations are also included in Table 2 for comparison. The analytical model calculations employed the experimentally determined value of $\delta = 23.5^\circ$ for α -cristobalite [23] ($\phi = 0$ for α -cristobalite). The CTM1 values were calculated assuming a 'strength' parameter of $\kappa = 5.18$ from the parametric fit to the Poisson's ratio for loading along x_3 (ν_{31}), for which the CTM1 has been shown to be a valid model. A value of the strength parameter $\lambda_1 = 35$ was found to give the best agreement of the CTM2 to the combined experimental ν_{12} and ν_{13} values. The CTM3 gives the exact values for both ν_{12} and ν_{13} when $\lambda = 15.1$ and $\kappa = 2.02$.

4 Discussion

The experimental unit-cell dimensions for α -cristobalite are $X_1 = 4.978$ Å and $X_3 = 6.948$ Å [24], which compare with the predicted undeformed values of $X_1 = 4.982$ Å and $X_3 = 6.658$ Å from the simulations reported here (Fig. 6a). The predicted value for X_1 is, therefore, in excellent agreement with experiment. The value of X_3 is underestimated in the simulations by 5%. The predicted values are similar to those from the pair potential calculations of Keskar and Chelikowsky [25] who reported predicted values of $X_1 = 4.96$ Å and $X_3 = 6.68$ Å.

Experimental unit-cell dimensions for ordered β -cristobalite have been reported by Peacor [30]: $X_1 = 5.07$ Å and $X_3 = 7.17$ Å, which compare with the predicted values of $X_1 = 4.84$ Å and $X_3 = 7.47$ Å from the simulations reported here (Fig. 6a). The predicted values are, therefore, accurate to $\pm 5\%$ of the experimental values, which is consistent with the level of agreement found in the simulations for the α -phase (X_3 dimension). However, the predicted values correspond to an applied stress of 1.2 GPa along the x_3

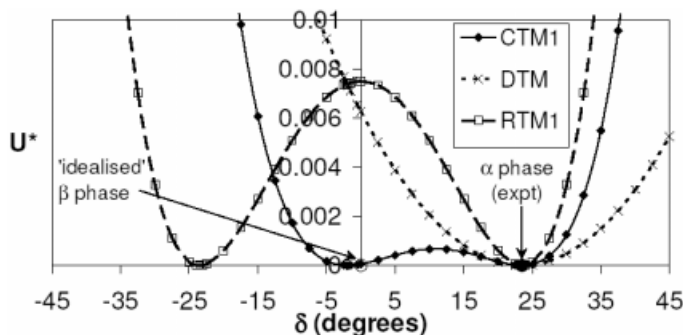


Fig. 7 Normalised strain energy (U^*) vs. tilt angle (δ) predictions [13, 31] from the DTM, RTM1 and CTM1 ($\kappa = 5.18$) for cristobalite ($\delta_\alpha = 23.5^\circ$).

direction, and so it is expected that the predicted X_3 value should be greater than the undeformed value. In fact, at an applied load of 1.2 GPa along x_3 the predicted Young's modulus in the loading direction was calculated to be $E_3 = 112$ GPa. The molecular model simulations showed linear stress-strain behaviour for both the α and β phases over the strain ranges considered here (a few % strain). Hence, the combination of stress and Young's modulus for β -cristobalite at the predicted transition stress of 1.2 GPa yield a strain of $\sim 1\%$ with respect to undeformed β -cristobalite (assuming linear elastic behaviour as shown in the molecular model simulations). This implies an undeformed value of $X_3 = 7.39 \text{ \AA}$ is predicted from the force-field simulations, which is in better agreement with the experimental value.

The Molecular Mechanics prediction of a σ_3 -induced transition from α -cristobalite to 'ordered' β -cristobalite with tensile load along x_3 is consistent with the prediction of a phase transformation from consideration of the analytical CTM1 model. Figure 7 shows the normalised strain energy function ($U^* = 2U/E_3$, where U is the strain energy and E_3 is the Young's modulus in the x_3 direction) plotted against tetrahedral tilt angle δ for the DTM, RTM1 and CTM1 analytical models (taken from Refs. [13, 31]). The CTM1 model predicts a second stable phase exists with a tilt angle in reasonable agreement with that for 'idealised' and 'ordered' β -cristobalite ($\delta = 0$).

A change in the sign of the Poisson's ratio ν_{21} is predicted in the Molecular Mechanics simulations to accompany the σ_3 -induced phase change (Fig. 6(b)). A change in the sign of Poisson's ratio at the phase transition has also been predicted using the analytical CTM1 model for the cristobalite structure [21], and has been observed in other materials (e.g. the Poisson's ratio of poly(N-isopropylacrylamide)/water gel has been observed to flip from a negative to a positive value at the volume phase transition [31]).

Previously, the analytical model of concurrent tetrahedral a -axes rotation and dilation (CTM1) has been found to be sufficient to predict the Poisson's ratio for loading of α -cristobalite in the x_3 direction, and in so doing contains the essential features of the deformation mechanisms in this case. However, the CTM1 cannot predict the Poisson's ratios sufficiently well for transverse loading of α -cristobalite, indicating that the CTM1 does not adequately describe the deformation mechanisms for loading along x_1 or x_2 . The data in Table 2 clearly show improved agreement in the transverse Poisson's ratios is achieved by incorporating the tetrahedral c -axes rotation mechanism into the models. The RTM2 model (deformation due to tetrahedral c -axes rotation only) correctly predicts the sign of ν_{12} to be positive, whereas the previously developed analytical models consistently predict $\nu_{12} = -1$. Incorporating tetrahedral c -axes rotation with concurrent dilation of the tetrahedra (CTM2) leads to an improved fit for both ν_{12} and ν_{13} to be possible (correct sign and improved agreement in the magnitude of the Poisson's ratio values). However, an exact fit for both ν_{12} and ν_{13} can be achieved by incorporating tetrahedral a -axes rotation to act concurrently with both tetrahedral c -axes rotation and dilation (CTM3).

In comparison, whilst the previous Burchart and BKS force-field simulations indicate low values of ν_{13} , they (and the Universal force-field) predict positive values for both ν_{12} and ν_{13} (Table 2). Only the

CVFF force-field correctly predicts both a positive sign for ν_{12} and a negative sign for ν_{13} , being in closer agreement with experiment than the analytical CTM2 model, but not as close as the analytical CTM3 model.

5 Conclusions

Analytical and Molecular Mechanics models have been used to investigate the structure-property relationships of the naturally-occurring auxetic nanomaterial α -cristobalite. The Molecular Mechanics models indicate the presence of a σ_3 -induced second phase corresponding to the ordered β -cristobalite geometry. The phase transition is predicted to be accompanied by a significant change in the magnitude of the on-axis Poisson's ratios, including a change in sign of at least one of the on-axis Poisson's ratios. The phase change and associated Poisson's ratio variations are in broad agreement with the predictions from the CTM1 analytical model (concurrent tetrahedral dilation and a -axis rotation).

Based on previous Molecular Mechanics simulations showing a divergence of the intertetrahedral angles with applied stress along the x_1 direction, analytical models have been developed to incorporate cooperative tetrahedral rotation about the local c -axes. Parametric fits of the new and previously developed analytical models suggest that α -cristobalite deforms by:

- 1 RUM (cooperative a -axis rotation) and tetrahedral dilation for uniaxial loading along the x_3 direction,
- 2 RUMs (cooperative a -axis and c -axis rotations) and tetrahedral dilation for uniaxial loading along the x_1 direction.

Acknowledgements The authors would like to thank the EPSRC for funding this work.

References

- [1] K. E. Evans, M. A. Nkansah, I. J. Hutchinson, and S. C. Rogers, *Nature* **353**, 124 (1991).
- [2] A. Alderson, J. Rasburn, S. Ameer-Beg, P. G. Mullarkey, W. Perrie, and K. E. Evans, *Ind. Eng. Chem. Res.* **39**, 654 (2000).
- [3] J. N. Grima, R. Jackson, A. Alderson, and K. E. Evans, *Adv. Mater.* **12**(24), 1912 (2000).
- [4] K. W. Wojciechowski, *Mol. Phys.* **61**, 1247 (1987).
- [5] L. J. Gibson and M. F. Ashby, *Cellular Solids: Structure and Properties* (Pergamon Press, London, 1988).
- [6] K. E. Evans, A. Alderson, and F. R. Christian, *J. Chem. Soc. Faraday Trans.* **91**(16), 2671 (1995).
- [7] He. P. Liu, and A. C. Griffin, *Macromolecules* **31**, 3145 (1998).
- [8] A. Alderson and K. E. Evans, *Phys. Rev. Lett.* **89**(22), 225503-1 (2002).
- [9] Y. Yeganeh-Haeri, D. J. Weidner, and J. B. Parise, *Science* **257**, 650 (1992).
- [10] H. J. McSkimin, P. Andreatch Jr., and R. N. Thurston, *J. Appl. Phys.* **36**, 1624 (1965).
- [11] F. S. Tautz, V. Heine, M. T. Dove, and X. Chen, *Phys. Chem. Miner.* **18**, 326 (1991).
- [12] M. T. Dove, K. D. Hammonds, V. Heine, R. L. Withers, Y. Xiao, and R. J. Kirkpatrick, *Phys. Chem. Miner.* **23**, 56 (1996).
- [13] A. Alderson, K. L. Alderson, K. E. Evans, J. N. Grima, and M. Williams, *J. Metastable Nanocryst. Mater.* **23**, 55 (2004).
- [14] E. Vos Burchart, *Studies on Zeolites: Molecular Mechanics, Framework Stability and Crystal Growth*, Ph. D. Thesis, Delft University of Technology (The Netherlands 1992), Table 1, Chap. XII.
- [15] R. W. G. Wyckoff, *Amer. J. Sci.* **9**, 448 (1925).
- [16] W. Nieuwenkamp, *Z. Kristallogr.* **96**, 454 (1937).
- [17] M. Hatch and S. Ghose, *Phys. Chem. Miner.* **17**, 554 (1991).
- [18] J. Leadbetter, T. W. Smith, and A. F. Wright, *Nature* **244**, 125 (1973).
- [19] F. Wright and A. J. Leadbetter, *Philos. Mag.* **31**, 1391 (1975).
- [20] M. O'Keeffe and B. G. Hyde, *Acta Cryst. B* **32**, 2923 (1976).
- [21] A. Alderson and K. E. Evans, *Phys. Chem. Miner.* **28**, 711 (2001).
- [22] A. Alderson, M. R. Williams, P. J. Davies, K. L. Alderson, and K. E. Evans, in preparation 2004.
- [23] J. J. Pluth, J. V. Smith, and J. Faber Jr., *J. Appl. Phys.* **57**, 1045 (1985).

- [24] W. A. Dollase, *Z. Kristallogr.* **121**, 369 (1965).
- [25] N. R. Keskar and J. R. Chelikowsky, *Phys. Rev. B* **46**, 1 (1992).
- [26] W. H. van Beest, G. J. Kramer, and R. A. van Santen, *Phys. Rev. Lett.* **64**, 1955 (1990).
- [27] K. Rappe, C. J. Casewit, K. S. Colwell, W. A. Goddard, and W. M. Skiff, *J. Am. Chem. Soc.* **114**, 10046 (1992).
- [28] K. Rappe and W. A. Goddard, *J. Phys. Chem.* **95**, 3358 (1991).
- [29] Force-Field Based Simulations Cerius² User Guide (MSI Inc., San Diego, USA, 1996).
- [30] R. Peacor, *Z. Kristallogr.* **138**, 274 (1973).
- [31] A. Alderson and K. E. Evans, *Phys. Rev. B*, submitted 2004.
- [32] S. Hirotsu, *J. Chem. Phys.* **94**, 3949 (1991).